Key Points:
- Slip history of 2014 Napa earthquake is constrained with strong motion records
- An isolated, high stress drop, small subevent excited the largest PGA
- Rise time gradually increases when rupture propagates to shallower depth

Correspondence to:
C. Ji,
ji@geol.ucsb.edu

Rupture history of 2014 M_w 6.0 South Napa earthquake inferred from near-fault strong motion data and its impact to the practice of ground strong motion prediction

Chen Ji[1,2], Ralph J. Archuleta[1,2], and Cedric Twardzik[1,2]

[1]Earth Research Institute, University of California, Santa Barbara, California, USA, [2]Department of Earth Science, University of California, Santa Barbara, California, USA

Abstract The spatiotemporal rupture history of the 2014 South Napa earthquake is constrained using near-fault strong motion records. An aggressive source parameterization with 1372 subfaults is adopted to match the signals in the transverse components up to 4 Hz. The result reveals that the rupture of the Napa earthquake initiated at a depth of 9.84 km and propagated mainly to north-northwest (NNW) and updip on a 13 km long fault patch. A gradual increase in average rise time when the rupture propagates to shallower depth is observed. However, it is the rupture of a small (M_w 4.9), isolated, and high stress drop fault patch that excited the largest ground acceleration at stations south of the epicenter. Such fine-scale rupture heterogeneity shall be considered during seismic hazard analysis.

1. Introduction

The 24 August 2014 M_w 6.1 South Napa earthquake initiated at 3:20 A.M. local time near the city of Napa, California. The relocated U.S. Geological Survey (USGS) hypocenter [*Hardebeck and Shelly*, 2014] is at 38.203°N, −122.308°E at a depth of 9.84 km (Figure 1). It is the largest earthquake in the San Francisco Bay area since the 1989 M_w 6.9 Loma Prieta earthquake. Field investigations [e.g., *Hudnut et al.*, 2014; *Trexler et al.*, 2014] revealed that this earthquake occurred on the south-southeast (SSE) oriented West Napa Fault. Preliminary finite fault studies based on distant strong motion data or local GPS vectors show that the rupture propagated unilaterally updip and to the NNW for about 15 km [*Barnhart et al.*, 2015; *Dreger et al.*, 2015]. The rupture reached the surface with a maximum slip of 0.46 m (Figure 1) [*Hudnut et al.*, 2014]. This earthquake was followed by a moderate aftershock sequence with only five $M > 3$ aftershocks within the first 3 months (Figure 1) (http://www.ncedc.org) but had large postseismic deformation at the surface [e.g., *Hudnut et al.*, 2014].

The Napa earthquake produced one of the best strong motion data sets for the class of magnitude 6 earthquakes. Preliminary analysis of this data set indicated that relative to the ground motion prediction equation of *Boore and Atkinson* [2008], the South Napa earthquake had much higher peak ground accelerations (PGAs) and peak ground velocities (PGVs) in the near-fault region but systematically lower PGAs and PGVs at distant sites (>30 km) (Figure S1 in the supporting information), (http://www.strongmotioncenter.org). To better understand the cause of this discrepancy, we constrain the rupture model of the South Napa earthquake using the waveforms recorded at near-fault strong motion stations.

2. Data Process, Velocity Model, Fault Geometry, and Inversion Method

We have selected the strong motion records at 21 near-fault stations (Figure 1). Their epicentral distances are less than 35 km. We integrate the acceleration to velocity and high-pass filter above 0.05 Hz to suppress the long-period noise. We rotate the horizontal components to the corresponding radial (R) and transverse (T) components relative to the epicenter. Figure 2 shows the T components. Note the two narrow pulses recorded by stations south of the epicenter (with azimuths from 149° to 213°, Figure 2). The pulses have widths of 0.3 to 0.4 s and are separated by 1.7–1.8 s. At the stations west of the hypocenter, such as NTO and NSP, similar double pulses can be seen as well, but the second pulse is much wider (>1.5 s). Because many large near-fault outliers of the ground motion predictions are associated with these double pulses, we attempt to locate their corresponding sources. In this study, after inspecting the waveform fits of preliminary
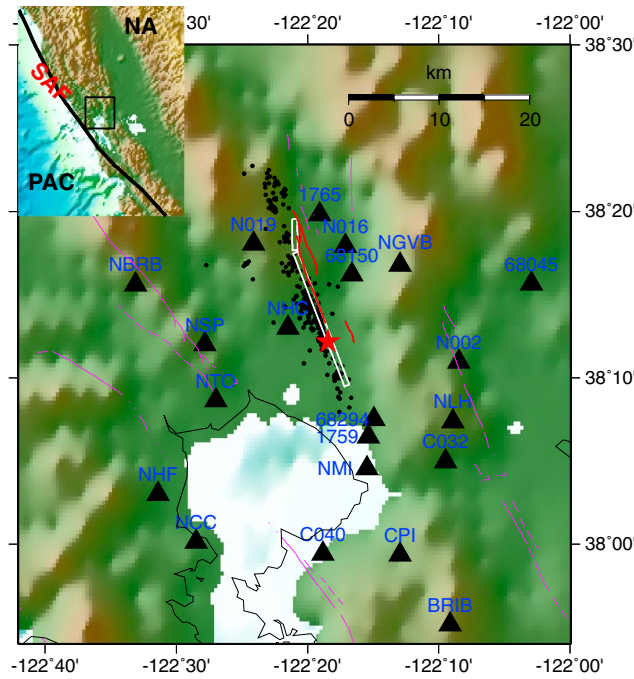
Figure 1. Background information for the 2014 South Napa earthquake. The black rectangle in the upper inset shows the study area. The red star and white lines denote the relocated epicenter and the surface fault trace of the South Napa earthquake, respectively. Narrow white boxes show the surface projections of the fault segments used; the black dots indicate the epicenters of the relocated aftershocks. The black triangles show the locations of 21 strong motion stations.

inversions we constrain the preferred slip model by matching the signals for the transverse components up to 4 Hz; for radial and vertical components, we attempt to fit the signals only up to 1.25 Hz.

We adopt 1-D GIL7 crustal model (Figure S2) [*Stidham et al.*, 1999] to approximate the local Earth structure and calculate the Green's functions using the FK code written by *Zhu and Rivera* [2002]. While many previous studies suggested that the 3-D heterogeneity in this region is significant [e.g., *Hardebeck et al.*, 2007], its impact on the inverted source model could be reduced by properly aligning the observed waveforms. The details of our alignment procedure are discussed in the supporting information.

We approximate the causative fault geometry with two subvertical rectangular fault segments based on the surface fault trace and the relocated USGS hypocenter. Fault segments I and II have same fault dip angle (87°) and downdip extension
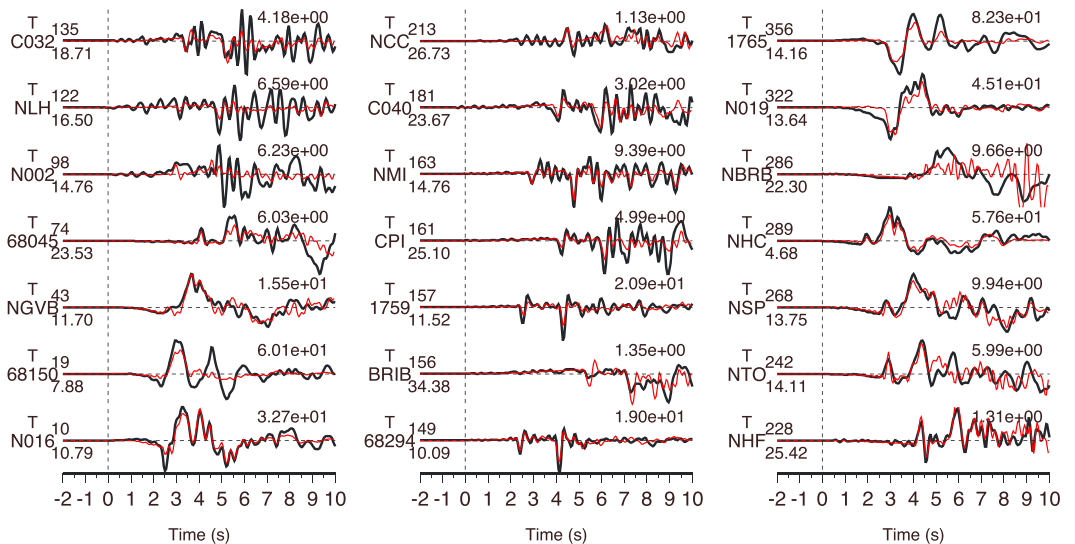
Figure 2. Comparison of observed velocity waveforms of the transverse components (black lines) and synthetic seismograms (red lines) computed using the preferred slip model. The waveforms have been band-pass filtered from 0.05 Hz to 4 Hz before the comparison. Only the first 10 s after *P* wave arrivals (dotted lines) are presented to highlight the fits to the body waves. For each comparison, the value above the beginning of the trace is station azimuth relative to the epicenter and the value below is epicentral distance. The value above the end of the trace is the observed peak amplitude in cm/s, which is used to normalize both synthetic seismogram and observation.
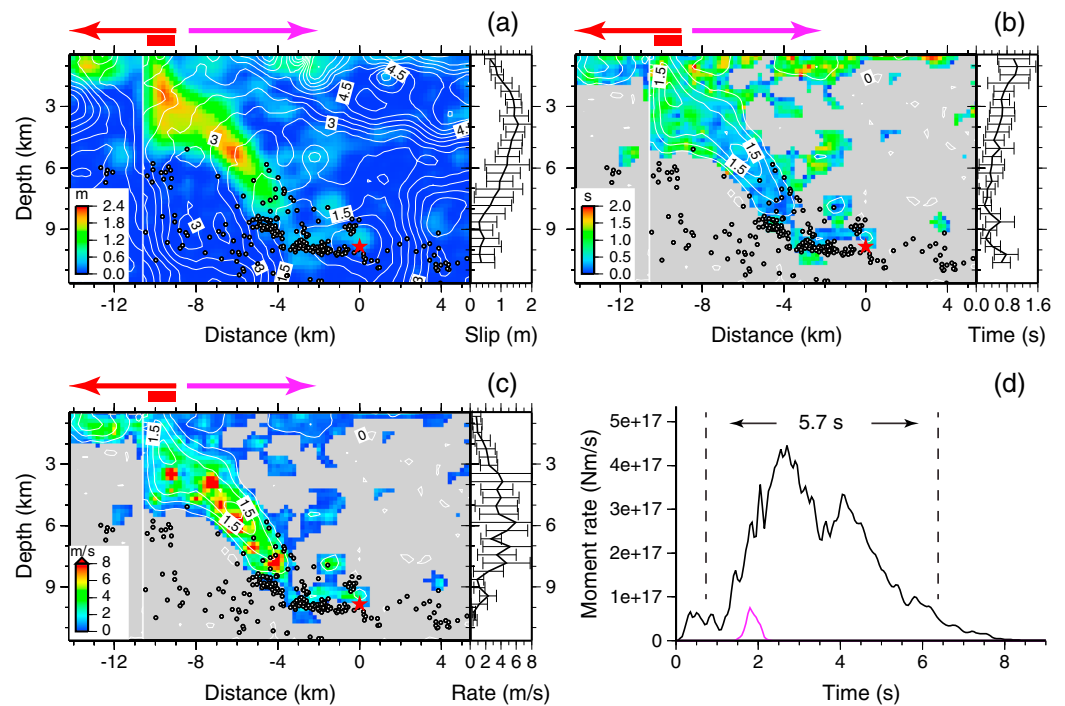
Figure 3. Summary of the preferred slip model. (a) Cross section of the slip distribution. The white vertical line indicates where the fault changes strike. The color denotes the slip amplitude, and white contour lines indicate the rupture initiation time. The black dots are the relocated aftershocks projected onto the fault. Depth profile of weighted average slip and its standard deviation are shown on the right. A red bar shows the locations where coseismic surface slips were more than 0.45 m. The large red and pink arrows highlight the surface regions with dominant coseismic or postseismic slips, respectively [*Hudnut et al.*, 2014]. (b) Cross sections of the rise time distribution. The contours with an interval of 0.5 m are used to show the fault slip; color denotes the value of rise time. The gray color is specifically used for subfaults, which have slip less than 10% of the peak slip. Depth profile of weighted average slip and its standard deviation are shown on the right. (c) Similar to Figure 3b but for average slip rate. (d) Moment rate function for the entire rupture (black line). The pink line is the moment rate for the P2 slip patch. See text for details.

(11.2 km) but different strike angles (N159°E and N179°E, respectively) and along-strike extensions (16 km and 3.2 km, respectively). The top edges of fault segments are 0.5 km below the surface (Table S1). To properly constrain the radiation of a heterogeneous slip distribution, the subfault size cannot be larger than one half of the shortest S wave wavelength we attempt to model [*Shao and Ji*, 2012]. According to the GIL7 model, in the depth range from 5 to 10 km, where we are most interested, the wavelength of a 4 Hz S wave is 0.85 km. We divide the two fault segments into 1372 subfaults (0.4 km × 0.4 km). A simulated annealing method is used to simultaneously invert for slip amplitude, rake angle, rupture initiation time, and the shape of an asymmetric slip rate function for each subfault by matching synthetics with the strong motion velocity waveforms in the wavelet domain [*Ji et al.*, 2002, 2003; *Shao et al.*, 2011]. The search ranges of each parameter are summarized in Table S2. The total number of unknowns in this study is 6860, which is larger than the total number of wavelet coefficients used (~6300). We stabilize the inversion by applying the Laplace smoothing constraints to the inverted fault slip and rupture initiation time [*Shao et al.*, 2011].

3. Inversion Results

Figure 2 shows the comparison of observations of the T components and synthetic seismograms predicted by our preferred model. Although waveforms of the first 25 s after the P arrivals were used in the inversion, a time window of 10 s is displayed here to highlight the fit to the beginning portion of the S wave. The rest of the waveform comparisons can be found in Figures S3 and S4. The double pulses recorded at southern stations are well modeled, although the synthetic amplitudes at some stations, such as 1759, are smaller than the observations. These amplitude differences might be caused by site amplification effects, which are station dependent. If this is indeed the case, our result suggests that the discrepancies among these stations are less than a factor of 2. However, the synthetic waveforms cannot explain the vertical and radial components (Figure S3)
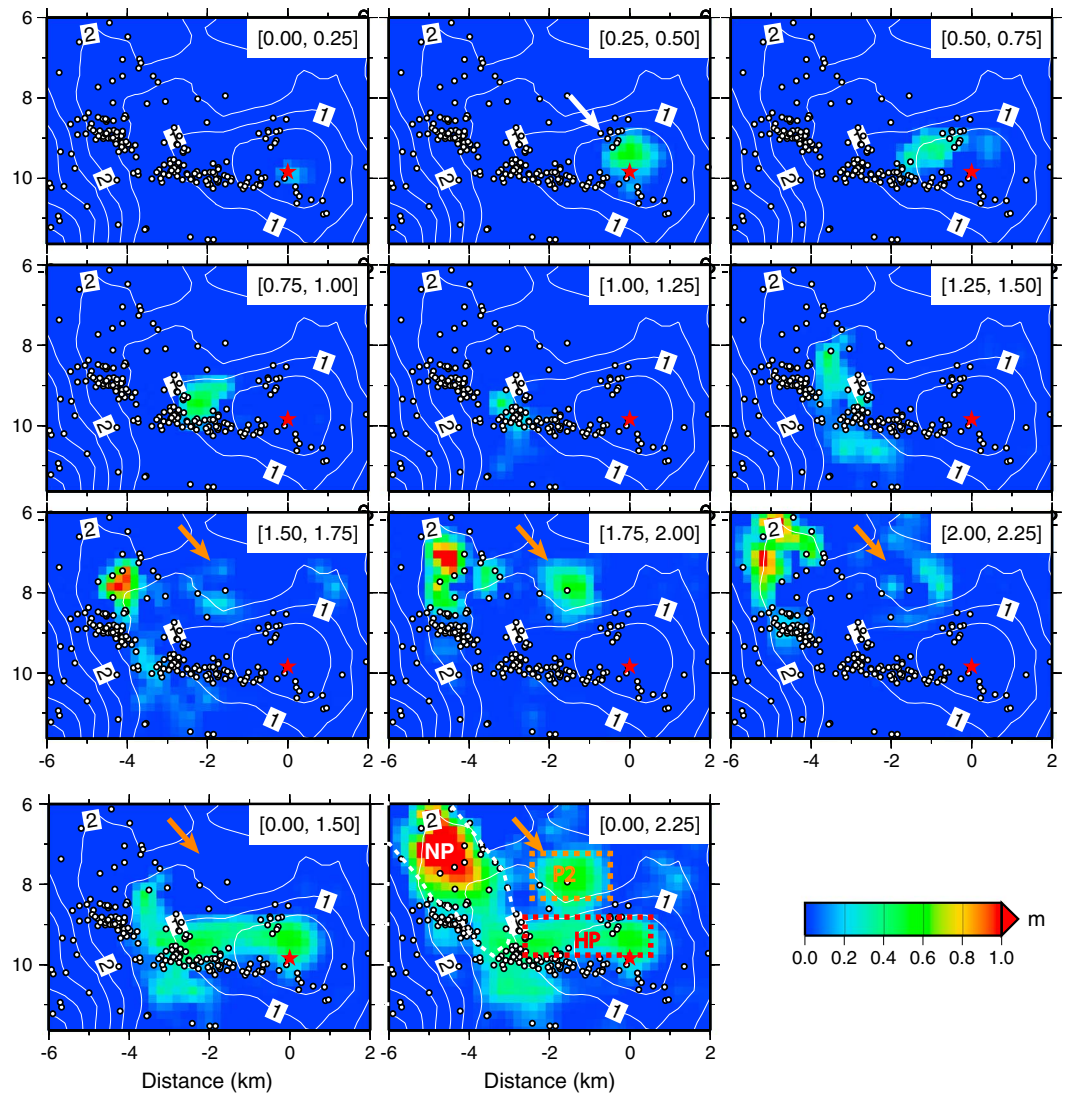
Figure 4. Snapshots of slip in 0.25 s intervals for the first 2.25 s of the Napa rupture. Figures are zooming on the region close to the hypocenter. The text gives the time window when the slip occurred. Color denotes the fault slip, and white contours show the rupture initiation time with an interval of 0.5 s. The red star denotes the hypocenter; circles show relocated aftershocks. The white and orange arrows are used to indicate the slip patches that produce the first and second velocity pulses, respectively. The cumulative slips during the first 1.5 s and 2.25 s are shown in the bottom row. Dashed lines in the last snapshot outline three high slip patches (HP, NP, and P2).

as well as the transverse. Although this is most likely caused by the unmodeled 3-D crustal structure, errors in fault geometry cannot be ignored. The synthetic seismograms for the radial and vertical components are more sensitive to small changes of the fault dip for a near-vertical strike-slip fault. It will be a task in the future to constrain the model with more accurate 3-D Green's functions and fault geometry.

3.1. Average Values of Kinematic Parameters

The preferred fault model for the 2014 South Napa earthquake has a cumulative seismic moment of 1.28×10^{18} Nm during its 8 s of coseismic rupture. The rupture has an average rupture velocity of 3.0 km/s and a peak slip of 2.24 m. Figures 3a–3c show the spatial distributions of slip, rise time, and average slip rate, respectively. The slip rate (v) here is defined as the ratio of fault slip and rise time. For subfaults with negligible slip the inverted rise time is not reliable; in Figures 3b and 3c we only present the results associated with the subfaults that have slip larger than 10% of the peak slip. Our solution has a compact slip distribution. Only one third of the subfaults have slip larger than 10% of the peak slip. These subfaults have an average slip of

0.74 m and are responsible for 84% of the total seismic moment. The mean values of their rise times and slip rates are 0.64 s and 1.9 m/s, respectively.

Most of the subfaults with significant slip are parts of a large slip patch in fault segment I (Figure 3a). This ~13 km long patch obliquely extends from 9 to 10 km depth to the surface. Where it reaches the surface is exactly the place where the peak surface offset of 0.45–0.46 m was observed (red bar, Figure 3). To the NNW, this patch does not extend across the intersection of fault segments I and II. We hereafter refer to it as Napa (NP) patch. The slip in fault segment II is mainly concentrated within the top 2 km. Its cumulative seismic moment is 1×10^{17} Nm, 8% of the total seismic moment.

Somerville et al. [1999] regressed the empirical relations among the average slip ($\overline{D}$), rise time ($\overline{T}_r$), and seismic moment, $\overline{D} = 3.36 \times 10^{-5} M_0^{1/3}$ and $\overline{T}_r = 4.37 \times 10^{-7} M_0^{1/3}$, where M_0 is moment in Nm. Using the inverted seismic moment of the Napa earthquake, the empirical $\overline{D}$ and $\overline{T}_r$ are 0.36 m and 0.46 s, respectively. Both are much smaller than the estimates of the Napa earthquake (0.74 m and 0.64 s). If defining the far-field rupture duration as the smallest time over which 95% of the total moment is released [*Ekstrom and Engdahl*, 1989], the estimate for the Napa earthquake is 5.7 s using the moment rate function in Figure 3d. The half duration 2.85 s is larger than the empirical half duration 2.45 s predicted using the relation $T_h = 2.26 \times 10^{-6} M_0^{1/3}$ [*Ekstrom and Engdahl*, 1989; *Ekstrom et al.*, 2005]. On average, the South Napa earthquake with its seismic moment has larger slip, longer rise time, and slightly longer rupture duration.

3.2. Rupture Kinematic History

To investigate the sources of the double pulses, we focus on the kinematic rupture process of the Napa earthquake in the first 2.25 s. Figure 4 shows snapshots of the preferred Napa model during this period. The South Napa earthquake initiates energetically. The moment rate $\dot{M}_0(t)$ reaches its first peak of 6.6×10^{16} Nm/s at 0.35 s (Figure 3d). Approximating the rupture initiation as a circular crack with constant stress drop and rupture velocity, the dynamic stress drop σ_d is related to moment rate as $\dot{M}_0(t) = D(v_r)\sigma_d v_r^3 t^2$, where v_r is rupture velocity and $D(v_r)$ is a function that is near unity and weakly depends on the v_r [*Boatwright*, 1980; *Ellsworth and Beroza*, 1995]. For $v_r = 3.0$ km/s, the estimate of σ_d during the first 0.35 s is 20 MPa. Thus, the rapid moment acceleration in the initial stage suggests high stress drop. Because the far-field velocity is roughly proportional to the moment acceleration $\ddot{M}_0(t)$, this energetic starting phase excites the first of the double pulses.

The rupture propagates unilaterally to the NNW direction with a speed of about 3.0 km/s and breaks a rectangular (3.2 km × 0.8 km) slip patch in approximately 1 s (hereafter referred to as HP, Figure 4). Note that the cessation of the HP rupture temporally leaves a "valley" in the moment rate function at about 1.1 s (Figure 3d) and is spatially correlated with the locations of a cluster of aftershocks extending vertically (Figure 4). The cumulative seismic moment within the first second of rupture is 4.2×10^{16} Nm (M_w 5.0). The rupture on the NP patch (Figure 4) initiated immediately after the rupture of HP. However, there is a significant change in rupture propagation direction, filling the "holes" of the aftershock distribution (snapshots from 1.0 s to 2.25 s, Figure 4). The rupture of NP produces a long slope in the cumulative moment rate from about 1.0 s to 2.5 s (Figure 3d) and generates the second T pulse observed at stations NHC and NSP. As expected, their pulse widths are about 1.5 s.

At about 1.5 s when the rupture front on the NP patch has already migrated about 4.5 km away from the hypocenter, an isolated slip patch P2 (Figure 4), which is much closer to the hypocenter, breaks. Note that in the preceding 1.5 s the slip curves around the P2 patch before this happens (Figure 4). This earlier rupture raises the shear stress at P2's northern and bottom edges and promotes the rupture as illustrated by our kinematic model (Figure 4). Notice that the rupture of P2 propagates updip and south-southeast rather than north-northwest. Over 80% of its total seismic moment (2.6×10^{16} Nm, M_w 4.9) occurs in the short time 1.75 s to 2.00 s (Figure 3d). Both the rapid moment release and rupture directivity lead to the second sharp SH pulse at the stations south of the epicenter as shown in Figure S5. Though the resolution is limited, this rupture pattern mimics the "double encircling pincer movement" shown in dynamic simulations for the breaking of an isolated asperity [*Das and Kostrov*, 1983] and barrier model [*Dunham et al.*, 2003]. *Beroza and Spudich* [1988] reported a similar scenario during the rupture of 1984 M_w 6.2 Morgan Hill earthquake, a strike-slip event on the nearby Calaveras Fault. An isolated high stress drop slip patch, which is 14 km away from the hypocenter, ruptures when the surrounding fault has ruptured. It caused strong directivity back toward the hypocenter and produced a large late acceleration pulse at stations near the epicenter.

After 2.25 s, the rupture on the NP patch continuously propagates and reaches the top edge of fault at about 5 s (Movie S1). The cumulative moment rate reaches its peak at 2.5 s when the rupture front has moved to a depth about 5.5 km (Figure 3). The cumulative moment rate quickly starts decreasing at about 4.5 s. Besides the rupture of the NP patch, the slip after 4.5 s occurs on a slip patch in fault segment II as well as a patch around −3 km along strike on fault segment I. Both patches are shallower than 2 km.

Using the inverted slip model, we estimate the static stress drop (σ_s) of the Napa earthquake (Figure S6). The peak stress drops of NP, HP, and P2 patches are 54 MPa, 26 MPa, and 16 MPa, respectively. The average stress drop over the entire fault is 10 MPa, consistent with the global average stress drop for strike-slip earthquakes [*Allmann and Shearer*, 2009].

4. Discussions

In this study, we have used an aggressive source parameterization with 1372 subfaults and 6860 free parameters. Because the inverted slip distribution is highly compact, the number of unknowns used to represent the rupture of the fault area with significant slip, i.e., larger than 10% of the peak slip, is only about 2300, far fewer than the 6300 wavelet coefficients used. The overall solution is consistent with preliminary models [e.g., *Dreger et al.*, 2015] but is more compact spatially and therefore larger in slip. The quality of the solution is supported by the good correlation with relocated aftershocks (Figures 3 and 4). However, we have to admit that, in principle, the impact of unmodeled 3-D heterogeneities of local crustal structure could become larger when the rupture propagates away from the hypocenter.

In fault segment I, where most of the slip occurs, we notice some interesting depth-dependent patterns in rise time and slip rate distributions. Figure 3 shows the weighted average slip, rise time, and slip rate for each row of subfaults in fault segment I. Here the corresponding fault slip is used as a weight to highlight the variations associated with high slip patches. The weighted average slip is almost constant from 10.6 km to 9.4 km and then monotonically increases by more than a factor of 3 in the next 5.6 km. After reaching a peak of 1.56 m at 3.8 km, it decreases monotonically toward the surface. The weighted average slip for the entire fault is 1.1 m. In contrast, the weighted average rise time linearly increases from 0.2 s at 7.8 km depth to 1.0 s at 0.6 km depth. Below 7.8 km, the weighted average rise time varies rapidly with depth. The weighted average rise time of the entire fault is 0.64 s. The depth profile of the weighted average slip rate is characterized by a "plateau" between 3.2 km and 7.8 km. The mean of the weighted average slip rate in this depth range is 4.1 m/s. Such high slip rate suggests high dynamic stress drop (σ_d) [e.g., *Brune*, 1970; *Kanamori*, 1994], coincident with the high static stress drop (σ_s) in this depth range (Figure S5). The average slip rate gradually decreases to 0.8 m/s below the surface as a result of the decrease in fault slip and increase in rise time. In the deeper region, the slip rate changes rapidly with depth, following the change in the weighted average rise time.

The decrease in average slip at shallow depth is correlated with the decrease in wave speeds (Figure S2). It could be the result of inelastic deformation at shallow depth [*Kaneko and Fialko*, 2011]. The depth variation in rise time does not correlate with fault slip and might also reflect a fault zone property. Longer rise times in the shallow portion of the crust fault have been previously noticed in other strike-slip earthquakes and have been used to explain the paucity of seismicity and coseismic slip at shallow depth [e.g., *Ide and Takeo*, 1997]. However, we want to point out the large lateral variation associated with these depth-dependent relations (Figure 3). In particular, the slip rate at shallow depth (<2 km) shows a clear bimodal spatial distribution along the strike, with high and low slip rate regions separated laterally at −9 km (Figure 3c). Coincidentally, above the region with high slip rate, surface slip was dominated by coseismic slip (below red arrow in Figure 3). While above the region with low slip rate, the surface slip was dominated by afterslip (below the fuchsia arrow in Figure 3).

Our kinematic model sheds some light on the causes of the discrepancies between the predictions and observed peak ground motion. In the current ground motion prediction equations based on the self-similar earthquake model, the peak ground motion is assumed to be only associated with overall earthquake parameters such as total seismic moment and fault dimension. In contrast, the Napa rupture initiated at the edge of a high stress drop fault patch (M_w 5.0). Subsequent rupture triggered another isolated high stress drop slip patch (M_w 4.9). The rupture of these two patches released only ~5% of the total seismic moment but excited high-frequency double pulses at the stations south of the hypocenter. The pulses might be further amplified by complex near-surface structures and are associated with some of the largest outliers of the PGA

and PGV predictions. At sites that are several fault lengths away from the source, the source can be treated as a point source. High-frequency radiation can be associated with the average values of source parameters. Both the longer rise time and longer total duration mentioned above would lead to lower high-frequency radiation at such distant sites (Figure S1, http://www.strongmotioncenter.org). Thus, the South Napa earthquake is a good example that the isolated small slip patches can dominate the high-frequency radiation at local sites but have negligible impact in the far field. Such fine-scale rupture heterogeneities must be considered during ground motion predictions.

5. Conclusions

We constrain the rupture history of the 2014 South Napa earthquake using near-fault strong motion records. We use 1372 subfaults (0.4 km × 0.4 km) on two fault segments to parameterize the fault plane. We invert for the kinematic parameters using the velocity waveforms with frequency up to 4 Hz. We obtain a highly compact slip model with one dominant slip patch and multiple secondary slip patches. The cumulative seismic moment within 8 s of rupture is 1.28×10^{18} Nm or M_w 6.0. The rupture is associated with relatively larger average slip of 0.74 m, longer rise time of 0.63 s, and high-average slip rate of 1.9 m/s. In our model, rise time increases by a factor of 5 as the rupture propagates to the surface. In the end, we argue that the energetic rupture of small, isolated, and high stress drop fault patches should be considered in the seismic hazard analysis.

References

Allmann, B. P., and P. M. Shearer (2009), Global variations of stress drop for moderate to large earthquakes, *J. Geophys. Res.*, *114*, B01310, doi:10.1029/2008JB005821.

Barnhart, W. D., J. R. Murray, S.-H. Yun, J. L. Svarc, S. V. Samsonov, E. J. Fielding, B. A. Brooks, and P. Milillo (2015), Geodetic constraints on the August 2014 South Napa, CA earthquake, *Seismol. Res. Lett.*, *86*(2A), 335–343.

Beroza, G. C., and P. Spudich (1988), Linearized inversion for fault rupture behavior—Application to the 1984 Morgan-Hill, California, earthquake, *J. Geophys. Res.*, *93*(B6), 6275–6296, doi:10.1029/JB093iB06p06275.

Boatwright, J. (1980), Spectral theory for circular seismic sources—Simple estimates of source dimension, dynamic stress drop, and radiated seismic energy, *Bull. Seismol. Soc. Am.*, *70*(1), 1–27.

Boore, D. M., and G. M. Atkinson (2008), Ground-motion prediction equations for the average horizontal component of PGA, PGV, and 5%-damped PSA at spectral periods between 0.01 s and 10.0 s, *Earthquake Spectra*, *24*(1), 99–138.

Brune, J. N. (1970), Tectonic stress and spectra of seismic shear waves from earthquakes, *J. Geophys. Res.*, *75*(26), 4997–5009, doi:10.1029/JB075i026p04997.

Das, S., and B. V. Kostrov (1983), Breaking of a single asperity—Rupture process and seismic radiation, *J. Geophys. Res.*, *88*(Nb5), 4277–4288, doi:10.1029/JB088iB05p04277.

Dreger, D. S., M. H. Huang, A. Rodgers, T. Taira, and K. Wooddell (2015), Kinematic finite-source model for the 24 august 2014 South Napa, California earthquake from joint inversion of seismic, GPS and InSAR data, *Seismol. Res. Lett.*, *86*(2A), 327–334.

Dunham, E. M., P. Favreau, and J. M. Carlson (2003), A supershear transition mechanism for cracks, *Science*, *299*(5612), 1557–1559.

Ekstrom, G., and E. R. Engdahl (1989), Earthquake source parameters and stress-distribution in the Adak Island Region of the Central Aleutian Islands, Alaska, *J. Geophys. Res.*, *94*(B11), 15,499–15,519, doi:10.1029/JB094iB11p15499.

Ekstrom, G., A. M. Dziewonski, N. N. Maternovskaya, and M. Nettles (2005), Global seismicity of 2003: Centroid-moment-tensor solutions for 1087 earthquakes, *Phys. Earth Planet. Inter.*, *148*(2–4), 327–351.

Ellsworth, W. L., and G. C. Beroza (1995), Seismic evidence for an earthquake nucleation phase, *Science*, *268*(5212), 851–855.

Hardebeck, J. L., and D. R. Shelly (2014), Aftershocks of the 2014 *M*6 South Napa Earthquake: Detection, location, and focal mechanisms, Abstract S33F-4927 presented at 2014 Fall Meeting, AGU, San Francisco, Calif., 15–19 Dec.

Hardebeck, J. L., A. J. Michael, and T. M. Brocher (2007), Seismic velocity structure and seismotectonics of the eastern San Francisco Bay region, Calif., *Bull. Seismol. Soc. Am.*, *97*(3), 826–842.

Hudnut, K. W., etal. (2014), Key recovery factors for the August 24, 2014, South Napa earthquake U.S. Geological Survey Open-File Report 2014–1249, p. 51, doi:10.3133/ofr20141249.

Ide, S., and M. Takeo (1997), Determination of constitutive relations of fault slip based on seismic wave analysis, *J. Geophys. Res.*, *102*(B12), 27,379–27,391, doi:10.1029/97JB02675.

Ji, C., D. J. Wald, and D. V. Helmberger (2002), Source description of the 1999 Hector Mine, California, earthquake, Part I: Wavelet domain inversion theory and resolution analysis, *Bull. Seismol. Soc. Am.*, *92*(4), 1192–1207.

Ji, C., D. V. Helmberger, D. J. Wald, and K. F. Ma (2003), Slip history and dynamic implications of the 1999 Chi-Chi, Taiwan, earthquake, *J. Geophys. Res.*, *108*(B9), 2412, doi:10.1029/2002JB001764.

Kanamori, H. (1994), Mechanics of earthquakes, *Annu. Rev. Earth Planet. Sci.*, *22*, 207–237.

Kaneko, Y., and Y. Fialko (2011), Shallow slip deficit due to large strike-slip earthquakes in dynamic rupture simulations with elasto-plastic off-fault response, *Geophys. J. Int.*, *186*, 1389–1403.

Shao, G. F., and C. Ji (2012), What the exercise of the SPICE source inversion validation BlindTest 1 did not tell you, *Geophys. J. Int.*, *189*(1), 569–590.

Shao, G. F., X. Y. Li, C. Ji, and T. Maeda (2011), Focal mechanism and slip history of the 2011 M_w 9.1 off the Pacific coast of Tohoku Earthquake, constrained with teleseismic body and surface waves, *Earth Planets Space*, *63*(7), 559–564.

Somerville, P., K. Irikura, R. Graves, S. Sawada, D. Wald, Y. Iwasaki, T. Kagawa, N. Smith, and A. Kowada (1999), Characterizing crustal earthquake slip models for the prediction of strong ground motion, *Seismol. Res. Lett.*, *70*(1), 59–80.

Stidham, C., M. Antolik, D. Dreger, S. Larsen, and B. Romanowicz (1999), Three-dimensional structure influences on the strong-motion wavefield of the 1989 Loma Prieta earthquake, *Bull. Seismol. Soc. Am.*, *89*(5), 1184–1202.

JI ET AL.   2155

Trexler, C., A. Morelan, and M. Oskin (2014), Rapid mapping of surface rupture from the South Napa earthquake, Abstract S31G-01 presented at 2014 Fall Meeting, AGU, San Francisco, Calif., 15–19 Dec.

Zhu, L. P., and L. A. Rivera (2002), A note on the dynamic and static displacements from a point source in multilayered media, *Geophys. J. Int.*, *148*(3), 619–627.